Supplemental information for:

Patterns of precipitation change and climatological uncertainty among CMIP5 models, with a focus on the midlatitude Pacific storm track

Submitted to *Journal of Climate* May 2015

B. Langenbrunner, J. D. Neelin, B. R. Lintner, and B. T. Anderson

1 End-of-century *P* percent changes in CMIP5

Figures S1a,b show end-of-century P change calculated as a percent of the base period climatology. In general, the magnitude of percent increases in certain regions are substantially larger than percent decreases (as the latter should be bounded by -100%). Note also that these maps are for the MME mean, though several individual models give unphysical results, specifically with percent increases in the Sahel region and the central equatorial Pacific. These unrealistic percent values make EOF analysis difficult, which is discussed later in this supplement.

2 Methods

In the following subsections, we go into partial detail of the mathematics behind our analyses and refer the reader to a few helpful publications that discuss our techniques more comprehensively: Horel [1981], Wallace and Gutzler [1981], Richman [1986], and Hannachi et al. [2006] for EOFs or rotated EOFs; Bretherton et al. [1992] and Wallace et al. [1992] for coupled methods like MCA and correlation maps; von Storch and Zwiers [1999] and Wilks [2011] for textbook discussions of all of these methods, as well as alternatives.

2.1 EOF analysis for single variables

To aid in our explanation, let X be an $M \times N$ matrix consisting of all data from the ensemble, with M rows and N columns. Here, M is the number of models in the ensemble and N is the total number of grid points in the chosen domain, while the matrix X can represent the end-of-century changes for a field of interest at N grid points for all M models in the ensemble (e.g., end-of-century P changes in CMIP5). Furthermore, let X' be the ensemble matrix centered by the mean of each column of X (i.e., centered by the MME mean at each grid point). Finally, let $\mathsf{C} = (1/M)(\mathsf{X}'^T\mathsf{X}')$ be the $N \times N$ covariance matrix of the centered ensemble matrix.

To visualize leading modes of P change disagreement within the 36-model ensemble, we begin with global and regional EOF analyses on end-of-century P change fields, which amounts to an EOF analysis on the covariance matrix C. The decomposition yields a set of N eigenvectors, which are the modes of variability or disagreement across the ensemble of M models, as well as N corresponding eigenvalues, which give insight into the percent of overall variance in the ensemble that each mode accounts for. Note that in our analysis, the number of models M is typically much less than the number of grid points N; as a result, only the leading M eigenvalues and eigenvectors (out of N total) have any physical meaning (and we focus on the first two modes). Note that positive and negative values in modes should not be interpreted strictly as P increases or decreases, but rather model uncertainty in the exact placement of these increases and decreases—as well as the boundaries between them—relative to the MME mean.

Once the EOFs are obtained, we calculate an expansion coefficient for each model—equivalent to a principal component in traditional EOF analysis—by projecting that model's original P change map, centered by the MME mean at each grid point, onto the EOF mode of interest. This produces 36 different scalar expansion coefficients for the end-of-century EOF calculations, one for each model. The magnitude of each expansion coefficient represents the contribution of that specific model to the disagreement pattern; the larger the magnitude is for a given model, the more it contributes (either positively or negatively, relative to the MME mean) to intermodel uncertainty. We refer to these values as either expansion coefficients or model weights.

2.2 MCA for coupled modes of intermodel disagreement

We explore coupled modes of uncertainty between P and U-200 fields using maximum covariance analysis (MCA). MCA is a matrix decomposition performed on the cross-covariance matrix between two fields. As an example, let the matrix $\mathbf{P}$ be an $M \times N$ matrix of precipitation anomalies, for M models at N grid points. Let $\mathbf{U}$ be an $M \times K$ matrix consisting of zonal wind anomalies for M models at K grid points. Let $\mathbf{P}'$ and $\mathbf{U}'$ be the original matrices centered by their column means at each grid point and converted into standardized units. This standardization step prevents differences in units from affecting the results and is done by dividing the centered P data by the standard deviation of the P anomalies matrix (i.e., the standard deviation of P anomalies across all models simultaneously), and likewise for the centered U-200 data and $\mathbf{U}$ matrix. Finally, let $\mathbf{S} = (1/M)(\mathbf{P}'^T\mathbf{U}')$ be the $N \times K$ cross-covariance matrix between the two fields.

MCA calculates patterns explaining the maximum amount of covariance in a data set. MCA will factor the matrix $\mathbf{S}$ into three matrices, $\mathbf{S} = \mathbf{\Pi\Sigma Y}^T$. Columns in $\mathbf{\Pi}$ are referred to as left singular vectors, columns in $\mathbf{Y}^T$ are right singular vectors, and each pair has a singular value associated with it along the diagonal in the matrix $\mathbf{\Sigma}$. Each pair of singular vectors comprises a coupled mode of covariability between the two fields (i.e., coupled disagreement pattern between the two variables relative to the MME mean of each field).

For every pair of singular vectors, the singular value in $\mathbf{\Sigma}$ can be used to calculate the covariance fraction (CF) between the two fields in that mode. We choose to report this instead of the squared covariance fraction; see Cheng and Dunkerton [1995] for further discussion.

3 Global PUPs of *P* change disagreement

Figures S2 and S3 show the first and second PUPs from a global EOF analysis on P changes, for the DJF and JJA seasons, respectively. As noted in the main text, the acronym "PUP" (principal uncertainty pattern) is used interchangeably with "mode" and "pattern." To the right of each mode, we display the expansion coefficients for each ensemble, normalized to have unit variance so that a value of ± 1 on the vertical axis implies one standard deviation departure from the MME mean P change. In these results, global EOFs are computed over all latitudes, though the patterns are weak poleward of about 60°, and so we crop the maps slightly in the figures to show better detail.

In both seasons, the first few modes are dominated by model disagreement in P change within the tropics. For DJF, the first PUP (Fig. S2a) has a strong uncertainty signal in the western Pacific warm pool; the second PUP (Fig. 2b) reflects disagreement primarily in the amount of P decreases over the eastern flank of the SPCZ. For JJA, the first PUP (Fig. S3a) appears to highlight model disagreement in the position of the eastern Pacific ITCZ, though the entire tropics have patches of uncertainty of similar magnitude. The second PUP (Fig. S3b) is even more tropically confined, again showing disagreement in displacement of the ITCZ and showing continuous signal along convective margins throughout the Pacific Ocean basin.

3.1 Intermodel disagreement versus internal model variability

The expansion coefficients shown in Figs. S2c,d and S3c,d give a sense of how individual models contribute to the corresponding PUP. Each red point represents an individual run from the model on the horizontal axis and characterize total ensemble spread, a combination of internal variability and differences in the individual models' response to radiative forcing. In some cases, a few particular models are noticeable outliers and project strongly onto the global PUPs, but this is not consistent across seasons. There is, however, notable consistency among groups of models that are taken from the same modeling center. For example, the signs and magnitudes of the expansion coefficients show little variation among the three HadGEM2 models as well as the three IPSL models, and this is true in all seasons and PUPs. An exception would be the two BCC models, which have large expansion coefficients of opposite sign in the second DJF mode (Fig. S2d). The robustness of global PUPs against removing the BCC and/or CSIRO models is discussed in the next section.

The box and whisker plots on the right in Figs S2c,d and S3c,d show the overall spread of the red points. Note the red line within each box and whisker plot represents the median of the red points, and the horizontal zero line represents the MME mean. The sign of the median gives information about the model distribution about the MME mean for this given pattern, with a negative median indicating right skew (a longer tail in the positive direction), and a positive median indicating left skew.

Along with red points in Figs. S2c,d and S3c,d, the smaller black points give a sense of how internal model variability compares to intermodel spread. For a six models, we have downloaded additional ensemble runs from the CMIP5 database to calculate end-of-century P changes for each (see Table 1 for more detail), and these maps are projected onto the full-ensemble PUPs. Additional runs of a given model (black points) exhibit a variability range that is a small fraction of the intermodel spread (red points). More quantitatively, in both leading global modes and seasons, the variance of the black points for a given model is less than 5% of the entire ensemble variance, except for the CSIRO-Mk-3-6-0 model in the DJF season, which is about 13%. This is approximately true for the midlatitude Pacific storm track region as well (see the main text), though internal model variability is a slightly larger fraction.

3.2 EOFs of *P* change as a percent of the base period climatology

Given that global PUPs calculated on absolute P change are dominated by the tropics, it is useful to consider normalizing model P changes prior to EOF analysis in a way that could emphasize higher latitudes while down-weighting the tropical influence. One possible approach—dividing the P change at each grid point by the base period climatology—becomes difficult in practice because nearly half of the models in the ensemble show unphysical percent P increases on the order of $10^3\%$ or more, particularly in the Sahel region and the central equatorial Pacific.

Masking these unrealistic grid points also proves unfruitful. Figures S4 and S5 show PUPs where grid points with P changes outside of the range $[-100\%, +250\%]$ were masked prior to EOF analysis (and show up as white grid points in the figures). While this approach does allow one to see more detail on signals of intermodel uncertainty outside of the tropics, the criteria for masking are somewhat arbitrary, and the information one gains about regional uncertainty patterns from Figs. S4 and S5 relative to Figs. S2 and S3 does not increase substantially. We therefore focus on absolute P change PUPs in the main text and emphasize regional domain analyses.

3.3 Rotated EOFs

We have tested whether varimax EOF rotation [Kaiser, 1958] provides a clearer understanding of the P change PUPs in both the global and midlatitude Pacific storm track domains. Rotation of global modes does not clarify any disagreement patterns already evident in the local standard deviation plots and original EOFs. Rotation of the midlatitude Pacific storm track PUPs redistributes the jet extension and shift modes across the first three rotated modes, though this does not change our original interpretation. EOF rotation therefore confirms that the P change PUPs in Fig. 6 (main text) are meaningful and stable, though it does not help gain more regional information about model disagreement.

4 Testing the sensitivity of PUPs to removal of model outliers

We have calculated the robustness of global P change PUPs to removal of either the two BCC models, one CSIRO model, or all three together (shown in Figs. S6 and S7). We compare the resulting partial-ensemble PUPs with the original PUPs (Figs. S2 and S3) and quantify the similarity by means of a spatial correlation of leading modes (though this is a blunt tool, and a full analysis would require more advanced methods). Our results show that removing the CSIRO model tends not to affect the PUPs substantially, though removal of the BCC models does affect the results in certain modes and seasons.

For DJF, the first global PUP is fairly robust to the removal any of these models (spatial correlation of $r = 0.89$). Furthermore, the majority of the notable patterns seen in the first two global PUPs in Figs. S2 and S3 are still present in Figs. S6 and S7, though they appear to be redistributed across modes, and the spatial correlations are therefore quite low (see captions for details). We conclude that the global PUPs are most sensitive to removal of the two BCC models (with CSIRO removal contributing minimally), though one can still draw the major conclusions from the partial-ensemble PUPs: that global uncertainty patterns are tropically dominated; that the largest type of uncertainty involves P increases in the deep tropics; that these uncertainties occur along the edges of tropical convection zones and within the ITCZ.

When the same analysis is applied to the N. Pacific storm track region, the PUPs are fairly robust to removal of BCC and CSIRO models (spatial correlation values are between $r = 0.85$ and $r = 0.86$ for the first and second PUPs, respectively). Since the majority of our discussion in the main text concerns PUPs in the midlatitude Pacific storm track region, we mention the caveat of global modes and the influence of outlier models, but we choose to use PUPs from the full ensemble in the midlatitude Pacific context.

5 Relationships between *P* and the *U*-200 jet

As a final point, we investigate relationships between EOFs of U-200 in the Pacific storm track region and global modeled P fields in the GCMs. These maps give insight into where model uncertainties in storm track U-200 are associated with uncertainties in tropical and storm track P, and to what extent these resemble modes of internal P and U-200 variability.

Figures S8a,b show end-of-century P changes correlated with the expansion coefficients of U-200 change PUPs (as seen in the main text Figs. 4e,f). For the first mode, P change uncertainty in the midlatitude Pacific depicts a jet extension mode and is associated with uncertainty in the southern tip of the SPCZ (in the central Pacific, between the equator and $20°$S). There is also a region of strong correlation of opposite sign to the north, which may reflect localized uncertainties in the descending branch of the Hadley circulation associated with jet uncertainties. The second correlation map exhibits a poleward P shift pattern in the western-to-central midlatitude Pacific, with an associated tropical P change signal.

Figures S8c,d show P climatologies correlated with the expansion coefficients of U-200 climatology PUPs (as seen in the main text Figs. 8c,d). In the first mode (Fig. S8c), the storm track region displays a similar jet extension pattern, though the zero contour is displaced and associated tropical P signals are much more localized along the southeastward sloping SPCZ axis. Again, a region of significant correlation of opposite sign appears north of the equator and may reflect localized interaction with the Hadley cell. The second mode (Fig. S8d) exhibits a meridional P shift in the midlatitude Pacific storm track region, though the tropics look quite different from that of Fig. S8b, with a strong signal south of the equator along the 4 mm day^{-1} contours, as well as a signal of strong opposite sign over the Pacific warm pool.

Figures S8e,f show monthly P values correlated with the first two modes of internal U-200 variability in the midlatitude Pacific storm track region. Details of internal variability calculations are found in the caption, and the first two modes in U-200 variability (not shown) are extension and shift modes, in that order. P correlations with the first mode (Fig. S8e) reveal a jet extension pattern in the midlatitude Pacific, and this is associated with tropical signals of opposite sign on either side of the equator. The second mode correlation map (Fig. S8f) shows a possible shift in storm track P, though the WP dipole is absent, and a more central-to-eastern Pacific shift appears in its place, with associated tropical variability evident as another cross-equatorial dipole, this time concentrated over the western tropical Pacific and maritime continent.

We conclude that while intermodel uncertainty patterns for end-of-century change in the Pacific storm track region may qualitatively resemble those for the historical climatologies or internal variability, the underlying processes appear to be distinct. Our results show that change PUPs are not associated with internal model variability on decadal+ timescales, though there do appear to be similarities between uncertainties in the P/U-200 plots that are reminiscent of internal variability.

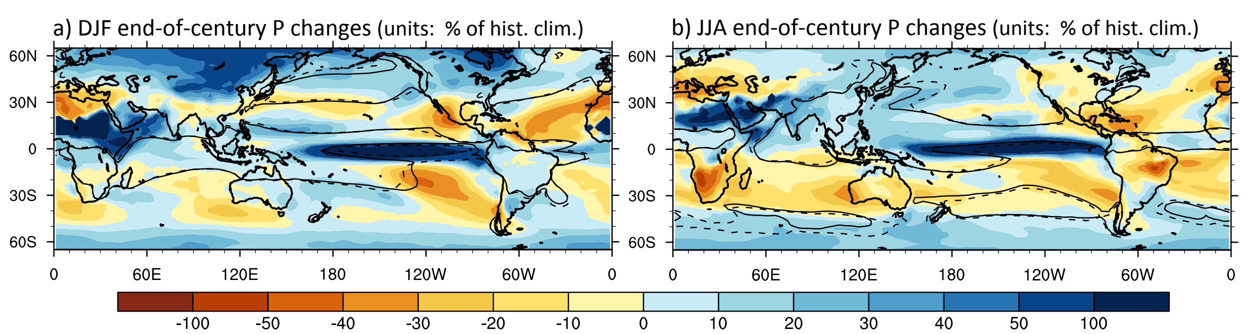

Figure S1: P change as a percent of the base period climatology at each model grid point, shown for (a) DJF and (b) JJA.

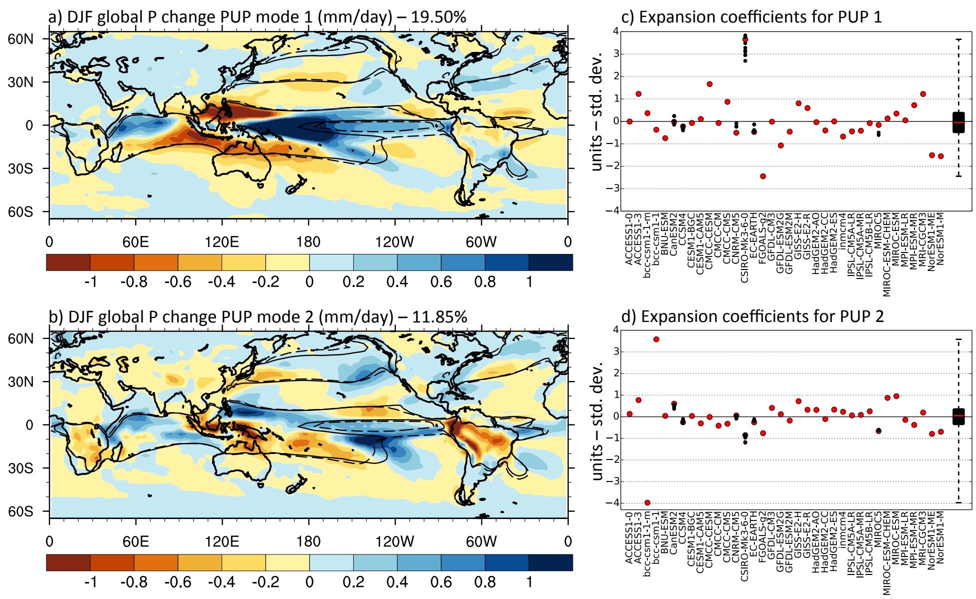

Figure S2: (a,b) First and second P change PUPs from a global EOF analysis on the 36-model ensemble P change maps, calculated for the DJF season in mm day^{-1}. Solid and dashed P contours are identical to those of Fig. 1 in the main text. The first PUP accounts for 19.50% of the total variance, and the second PUP and additional 11.85%. (c,d) Individual model expansion coefficients corresponding to the modes on the left, in units of standard deviation relative to the MME mean P change. Red and black dots and box and whisker plots are as described in the main text.

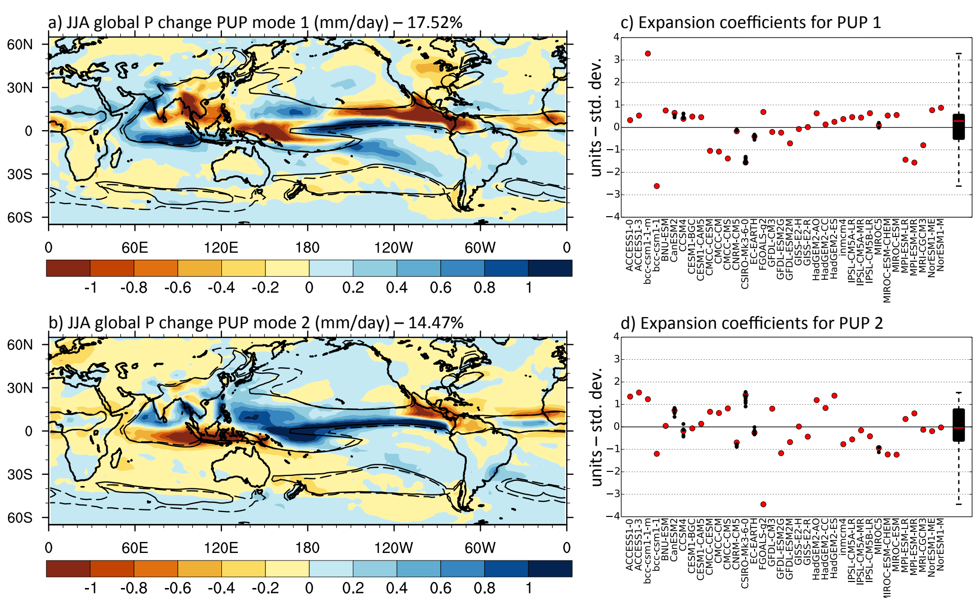

Figure S 3: As in Fig. S2, but for the JJA season. The first PUP for JJA accounts for 17.52% of the variance across the model ensemble, and the second PUP accounts for an additional 14.47%.

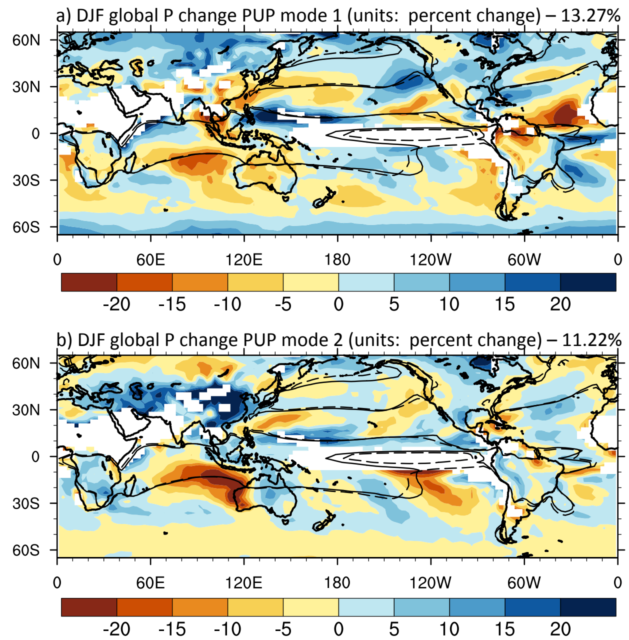

Figure S4: (a,b) First and second P change PUPs calculated over P changes as a fraction of the base period climatology for DJF. Areas with a P change outside of the range $[-100\%, +250\%]$ were masked prior to EOF analysis.

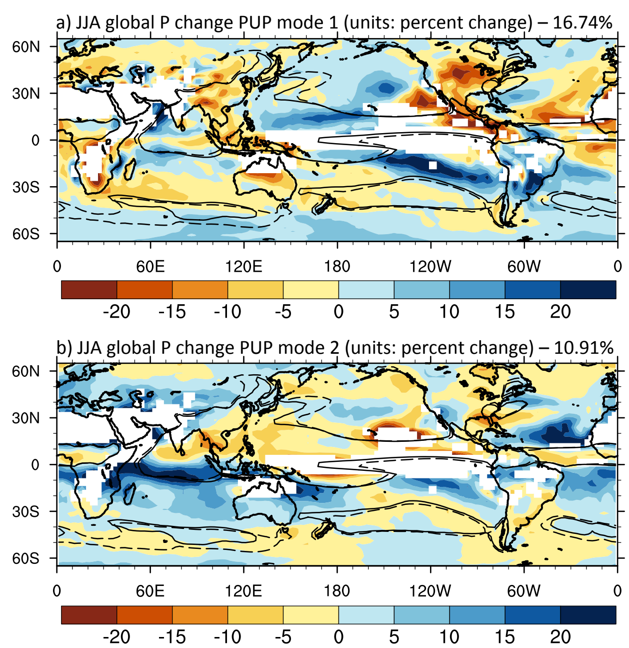

Figure S5: (a,b) Same as in Fig. S4 but for the JJA season.

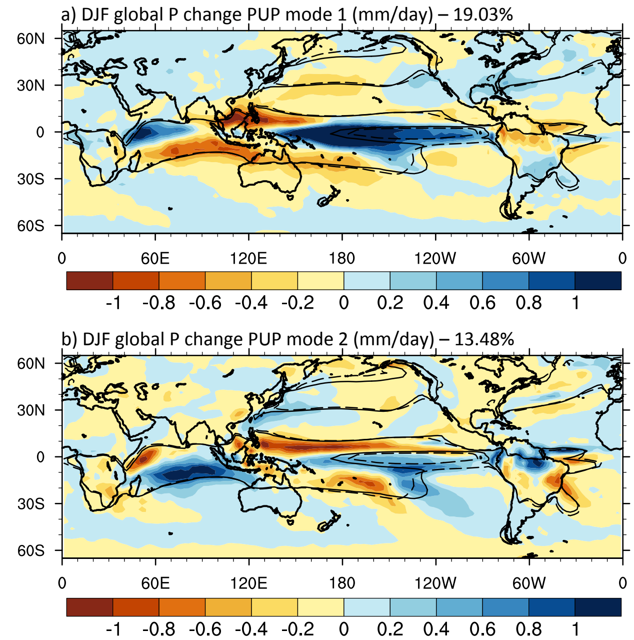

Figure S6: First and second DJF P change PUPs from a global analysis on a partial ensemble omitting the three models (bcc-csm1-1, bcc-csm1-1-m, and CSIRO-Mk3-6-0) with the most extreme expansion coefficients in Figs. S2 and S3. The magnitude of the spatial correlation between the first modes (Figs. S2a and S6a) is $r = 0.89$, and that for the second modes (Figs. S2b and S6b) is $r = 0.02$.

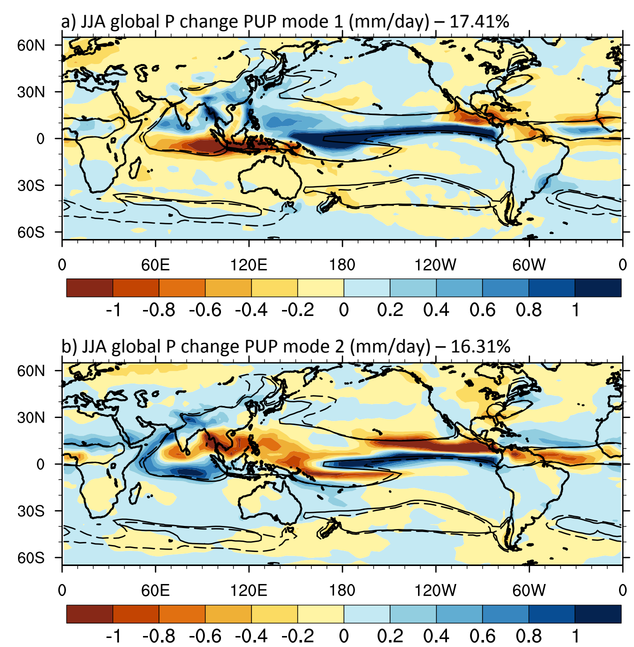

Figure S7: Same as in Fig. S4, but for JJA. The magnitude of the spatial correlation between the first modes (Figs. S3a and S7a) is $r = 0.11$, and that for the second modes (Figs. S3b and S7b is $r = 0.09$.

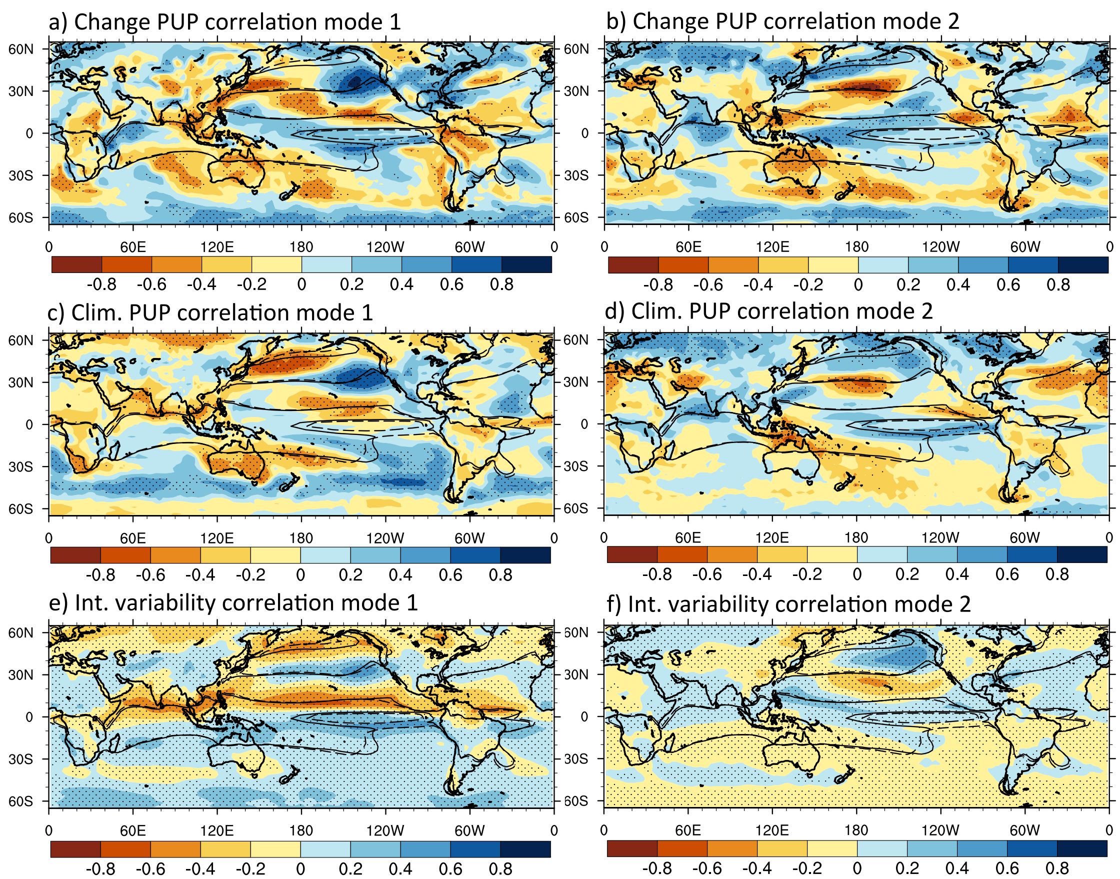

Figure S8: Correlations of P with U-200, normalized to mm day^{-1} for a standard U-200 deviation. (a,b) DJF P change values correlated with DJF U-200 change PUPs (as seen in Figs. 4e,f). (c,d) DJF model P climatologies correlated with expansion coefficients of U-200 climatology PUPs (as seen in Figs. 8c,d). (e,f) Monthly DJF P values correlated with internal U-200 variability in the storm track region for EOFs one and two. Stippling in all plots shows where the correlation passes a t-test at the 95% confidence level. Modes of internal U-200 variability were calculated using linearly detrended DJF values across all 36 models at once (here in the time dimension), with each model's climatology removed prior to analysis. The two leading patterns of internal jet variability in the storm track region represent (1) a jet extension (or pulsing) mode, which accounts for 40.95% of the total variability, and (2) a meridional jet shift (or wobbling) mode, accounting for an additional 15.35% (these patterns are not shown here but can be seen in other studies [see Delcambre et al., 2013, their Figs. 2a,b]).

References

C. S. Bretherton, C. Smith, and J. M. Wallace. An intercomparison of methods for finding coupled patterns in climate data. *Journal of Climate*, 5(6):541–560, 1992.

X. Cheng and T. J. Dunkerton. Orthogonal rotation of spatial patterns derived from singular value decomposition analysis. *Journal of Climate*, 8:2631–2643, 1995.

S. C. Delcambre, D. J. Lorenz, D. J. Vimont, and J. E. Martin. Diagnosing northern hemisphere jet portrayal in 17 cmip3 global climate models: Twentieth-century intermodel variability. *Journal of Climate*, 26(14):4910–4929, 2013.

A. Hannachi, I. T. Jolliffe, D. B. Stephenson, and N. Trendafilov. In search of simple structures in climate: simplifying eofs. *International Journal of Climatology*, 26(1):7–28, 2006.

J. D. Horel. A rotated principal component analysis of the interannual variability of the northern hemisphere 500 mb height field. *Monthly Weather Review*, 109(10):2080–2092, 1981.

H. Kaiser. The varimax criterion for analytic rotation in factor analysis. *Psychometrika*, 23(3):187–200, 1958.

M. B. Richman. Rotation of principal components. *Journal of Climatology*, 6(3):293–335, 1986.

H. von Storch and F. W. Zwiers. *Statistical analysis in climate research*. Cambridge University Press, 1999.

J. M. Wallace and D. S. Gutzler. Teleconnections in the geopotential height field during the northern hemisphere winter. *Monthly Weather Review*, 109(4):784–812, 1981.

J. M. Wallace, C. Smith, and C. S. Bretherton. Singular value decomposition of wintertime sea surface temperature and 500-mb height anomalies. *Journal of Climate*, 5(6):561–576, 1992.

D. S. Wilks. *Statistical methods in the atmospheric sciences*, volume 100 of *International geophysics series*. Academic Press, 3rd edition, 2011.

Table S 1: Models and affiliated modeling groups used in the analysis. When additional ensemble members were used for certain models, this is marked in the N_E column. When pre-industrial control runs are used to estimate internal model variability, the number of distinct 30-year intervals are reported in the N_{30} column. Asterisks mark the models for which direct atmosphere-only and coupled comparisons were made (25 total).

Coupled models	$\mathbf{N_E}$	$\mathbf{N_{30}}$	**Atmosphere-only models**	**Modeling center or group**
ACCESS1-0		16	ACCESS1-0*	Commonwealth Scientific and Industrial Research Organization and Bureau of Meteorology, Australia (CSIRO-BOM)
ACCESS1-3		16	ACCESS1-3*	
bcc-csm1-1-m		13	bcc-csm1-1-m*	Beijing Climate Center, China Meteorological Administration, Beijing, China (BCC)
bcc-csm1-1		16	bcc-csm1-1*	
BNU-ESM		18	BNU-ESM*	College of Global Change and Earth System Science, Beijing Normal University, Beijing, China (GCESS)
CanESM2	4	33	CanAM4*	Canadian Centre for Climate Modelling and Analysis, Québec, Canada (CCCMA)
CCSM4	5	35	CCSM4*	National Center for Atmospheric Research, Boulder, Colorado, USA (NCAR)
CESM1-BGC		16	—	
CESM1-CAM5		10	CESM1-CAM5*	
CMCC-CESM		9	—	Centro Euro-Mediterraneo per I Cambiamenti Climatici, Lecce, Italy
CMCC-CM		10	CMCC-CM*	
CMCC-CMS		16	—	
CNRM-CM5	4	28	CNRM-CM5*	Centre National de Recherches Météorologiques, Toulouse, France
CSIRO-Mk3-6-0	9	16	CSIRO-Mk3-6-0*	Commonwealth Scientific and Industrial Research Organization in collaboration with Queensland Climate Change Centre of Excellence, Victoria, Australia
EC-EARTH	5	14	EC-EARTH*	EC-EARTH consortium
FGOALS-g2		23	FGOALS-g2*	LASG, Institute of Atmospheric Physics, Chinese Academy of Sciences, Beijing, China
GFDL-CM3		16	GFDL-CM3*	NOAA Geophysical Fluid Dynamics Laboratory, Princeton, New Jersey, USA
GFDL-ESM2G		16	—	
GFDL-ESM2M		16	—	
—			GFDL-HIRAM-C180	
—			GFDL-HIRAM-C360	
GISS-E2-H		7	—	NASA Goddard Institute for Space Studies, New York, New York, USA
GISS-E2-R		18	GISS-E2-R*	
—			HadGEM2-A	Met Office Hadley Centre, United Kingdom (additional HadGEM2-ES realizations contributed by Instituto Nacional de Pesquisas Espaciais)
HadGEM2-AO		23	—	
HadGEM2-CC		7	—	
HadGEM2-ES		9	—	
inmcm4			inmcm4*	Institute for Numerical Mathematics, Moscow, Russia
IPSL-CM5A-LR		33	IPSL-CM5A-LR*	Institut Pierre Simon Laplace, Paris, France
IPSL-CM5A-MR		9	IPSL-CM5A-MR*	
IPSL-CM5B-LR		9	IPSL-CM5B-LR*	
MIROC5	2		MIROC5*	Japan Agency for Marine-Earth Science and Technology, Atmosphere and Ocean Research Institute (The University of Tokyo), and National Institute for Environmental Studies, Tokyo, Japan
MIROC-ESM-CHEM		8	—	
MIROC-ESM		17	—	
MPI-ESM-LR		33	MPI-ESM-LR*	Max Planck Institute for Meteorology, Hamburg, Germany
MPI-ESM-MR		33	MPI-ESM-MR*	
—			MRI-AGCM3-2H	Meteorological Research Institute, Tokyo, Japan
—			MRI-AGCM3-2S	
MRI-CGCM3		16	MRI-CGCM3*	
NorESM1-ME		8	NorESM1-ME*	Norwegian Climate Centre, Bergen, Norway
NorESM1-M		16	NorESM1-M*	